From the holdings of the Department of Special Collections , Princeton University Library, Princeton, NJ

These documents are either in the public domain, or can only be used for educational and research purposes (Fair use) as per U.S. Copyright law (text below). By accessing this file, all users agree that their use falls in the public domain or within fair use as defined by the copyrightlaw. We do not charge any permission or usage fees for the publication of images of material inour collections, including those provided by Princeton University Library, via our website, catalog, or directly from staff.For more information regarding copyright, credit, and citation please review the information onthe Copyright, Credit and Citation Guidelines page of our website.
https://library.princeton.edu/special-collections/policies/copyright-credit-and-citation-guidelines. If you have any questions, including how to order higher-quality images from the collection, contact Special Collections Public Services via our Ask Us! Form. https://library.princeton.edu/special-collections/ask-us

---

Master's Theses, 2022-2026 Electrical and Computer Engineering

2024

SUPPRESSING INTERFERENCE IN SPECTROSCOPIC SYSTEMS USING ABSORPTION MASKS

Mehta, Angela

Princeton, NJ : Princeton University

---

http://arks.princeton.edu/ark:/88435/dsp01xs55mg45q

U.S. Copyright law: The copyright law of the United States (Title 17, §108, United States Code) governs the making of photocopies or other reproductions of copyrighted material. Under certain conditions specified in the law, libraries and archives are authorized to furnish a photocopy or other reproduction. One of these specified conditions is that the photocopy or reproduction is not to be used for any purpose other than private study, scholarship, or research. If a user makes a request for, or later uses, a photocopy or reproduction for purposes in excess of fair use that user may be liable for copyright infringement. This institution reserves the right to refuse to accept a copying order if, in its judgment, fulfillment of the order would involve a violation of copyright law. https://www.copyright.gov/title17/title17.pdf

SUPPRESSING INTERFERENCE IN SPECTROSCOPIC SYSTEMS USING ABSORPTION MASKS

ANGELA MEHTA

MASTER'S THESIS
PRESENTED TO THE FACULTY
OF PRINCETON UNIVERSITY
IN CANDIDACY FOR THE DEGREE
OF MASTER OF SCIENCE

RECOMMENDED FOR ACCEPTANCE BY
THE DEPARTMENT OF ELECTRICAL
AND COMPUTER ENGINEERING

Advisor: Gerard Wysocki

May, 2024

©Copyright by Angela Mehta, 2024. All rights reserved.

Abstract

This thesis represents an ongoing research project in which absorption masks were used to reduce scattering in a Herriott multipass cell in a Wavelength Modulation Spectroscopy (WMS) system. To that end, this thesis presents some of the following steps to successfully see a scattering reduction in the absorption spectrum. It is organized in a few chapters and sets up a stage for the different methods implemented to tackle the scattering issue. This thesis, then, embarks on a discussion of the numerical method used for approximation. A discussion of various techniques used to simulate and design masks follows. The implementation of the mask in the experimental system is also analyzed. Finally, this thesis concludes with recommendations and the following steps to see a significant decrease in scattering in the optical cell.

Acknowledgements

I deeply thank my advisor, Gerard Wysocki, whose mentorship made this thesis possible. Thank you for wholeheartedly accepting me in the group and being a strong backbone throughout my time at Princeton. His patience and guidance have been of tremendous help to me.

To Michael, thank you for being a fantastic mentor and friend inside and outside the lab. You taught me much about research, leadership, and sportsmanship. I am very grateful for your patience and your time. Thank you so much!

To Nick, thank you for always helping me out in my time of need whether it reviewing presentations or thesis, you have been an immense help in my journey at Princeton. I truly appreciate your time and effort towards my work.

To Baichuan, sharing my love for the outdoors with you has been great. Thank you for playing tennis with me and for your encouragement when I needed them.

To the members of the PULSe lab, thank you so much for your support, advice, and friendship. I appreciate the feedback on my presentations and research work.

I want to thank my friends who have been my rock since day one at Princeton. Thank you for the fun adventures and advice. You are some of the most hardworking and loving people I have met. I will continue to cherish our memories lifelong.

This work wouldn't have been possible without the support of the Robotics Lab and the Princeton Department of Electrical and Computer Engineering. A big thanks to the ECE Administrators for being unconditionally supportive during my time at Princeton.

Lastly, I want to thank my family for their immense support and love in my journey at Princeton.

List of Figures

2.1 (Left) Diagram depicting beam coupling and coordinate axis of the Herriott type multi-pass cell. (Right upper) A simulated laser beam's spot pattern on a 3.6 m optical cell mirror is shown. (Right lower) Photograph of a mirror shown. 17

2.2 General schematic of a WMS system. The following pieces of instruments are used in the figure: function generator, temperature controller, laser current controller, oscilloscope, lock-in-amplifier, photodiode, multipass cell (MPC), and 30 dB attenuator. 18

2.3 Fabry-Perot Interferometer, using a pair of highly reflective, semi-transparent mirrors 19

2.4 Second harmonic signal of O_2 in ambient air. Spectra were averaged 100 times over ten s. 20

2.5 Spot positions for front and back mirrors using MATLAB. (Right) even spot patterns, including the first pass into the cell. (Left) There are odd spots with the 21st pass as the last pass. 22

2.6 Ray tracing of a laser beam in FRED. There are a total of 21 passes within the cell. 23

2.7 Spot pattern on the back mirror using FRED script. 23

2.8 This figure shows the difference between diffuse and specular reflection. Light is scattered in all directions when the rays hit dust particles or irregularities on the mirrors. 24
2.9 Point sources are located on the mirror corresponding to the spots' positions. Each point source is positioned at the center of the red squares. It's worth noting that the red squares indicate the selection of point sources clicking. 24
2.10 One of the point sources is turned on to see how it casts light uniformly and in all directions. The point source exhibits specific characteristics, including an angular spread cone of 20° and 500 angular zones over the angular spread. 25
2.11 Ray tracing of a laser beam to design mask. This process was iterated for each pass until all the rays passed through the holes. 26
2.12 This is a theoretical mask created to visualize a mask with zero scattered light contributed from neighboring spots. This is impractical, but getting as close to it as possible is the idea. 26
2.13 2 masks: one at 1/3 distance from the first mirror and the second one at 2/3 distance from the first mirror. 26
2.14 Irradiance distribution on an analysis plane in front of the back mirror with all point sources enabled. 78% decrease in scattered light after the addition of mask. 27
2.15 Total irradiance on an analysis plane for both front and back mirror. The mask is placed at different locations with all point sources turned on. 28
2.16 Mask 1.0 & 2.0's intensity distribution. Mask 2.0 blocks about 8% less scattered light than Mask 1.0. 29
2.17 A more simplified mask shown in FRED. Blocks about 8% less light than Mask 2.0 but easier to implement. 30

2.18 3-D printed mask is held in place with an optic mount within the Herriott multipass cell. 31
2.19 A more simplified mask shown in FRED. It blocks about 8% less light than Mask 2.0 but is easier to implement. 31
2.20 Transmission signal used to find the time values at dips. 32
2.21 O_2's absorption peaks at 13098.37 and 13100.82 cm^{-1}, corresponding to the transition frequencies found in the experiment. 33
2.22 Noisy part of no mask signal with x-axis in wavenumbers. 33
2.23 FFT of noisy signal with and without the mask. Normalized signal presenting distance components present in the fringes' signal. The signal is normalized to its DC component. 34
2.24 Histogram representing the number of noise instances corresponding to different distances in the system. The circled bin is for the multipass cell's path length of 17.1 cm. 35
2.25 Second harmonic signals with circled areas were used for SNR analysis. (left) Mask, (right) No mask 36

3.1 2 mask system where the masks are 1/3 and 2/3 distance apart from the front mirror. Blocks 87% more scattered light than Mask 1.0 in Figure 2.16a. 38
3.2 Spot pattern captured on the printer transparency paper using an iPhone. . 39

Contents

Abstract 3

Acknowledgements 4

List of Figures 5

1 Introduction 10

2 Wavelength Modulation Spectroscopy 12

2.0.1 Spectroscopic Modeling . . . 12

2.0.2 Molecluar Lineshape Background . . . 13

2.0.3 Gas Cell . . . 17

2.0.4 Experimental Method . . . 18

2.1 Optical Interference Noise in WMS Measurements . . . 19

2.2 Multi-Pass Cell Simulations . . . 21

2.2.1 Numerical Simulations of Multi-Pass Cell using MATLAB . . . 21

2.2.2 Ray Tracing Software . . . 21

2.3 Suppressing Scattering in Herriott Multipass Cell . . . 23

2.3.1 Simulating Scattering . . . 23

2.4 Mask Design and Optimization . . . 25

2.4.1 Design of a Mask Pattern and Placement . . . 25

2.4.2 Scattered Light Simulations with Mask . . . 27

2.4.3 Mask Placement 27
2.4.4 Optimization of Mask Design 28
2.5 Experimental Setup with Mask 30
2.5.1 Noise Analysis 33
2.5.2 SNR Analysis 35

3 Conclusions and Future Directions **37**

A Appendix **40**
A.1 FRED Scripts 40
A.2 MATLAB Code 45

Chapter 1

Introduction

This thesis is about increasing sensitivity in gas detection using a laser spectroscopy technique, wavelength modulation spectroscopy. Spectroscopy is the study of the interaction of light and matter, and it's widely used for detecting and quantifying species' concentrations in sensitive gas detection in industry and research. Gas sensing is essential because humans are surrounded by various types of gases in the environment or industrial processes. Some gases can be dangerous, so monitoring their concentration precisely is necessary. For example, carbon monoxide detectors warn early about gas leakage or a potential fire [1]. Spectroscopy monitors environmental gases such as carbon dioxide, nitrous oxide, and trace gases. Precisely measuring the concentration of these gases is essential for evaluating ecological conditions and executing effective countermeasures to mitigate their impact. For instance, methane, a potent greenhouse gas, contributes significantly to climate change, even at low atmospheric concentrations. Therefore, its precise detection and real-time measurements are important to understanding its role in the environment and making strategies to reduce its content [2].

Laser-based spectroscopy is widely used because it provides high sensitivity and real-time and remote measurements. Consequently, it is also utilized for real-time detection of pollutants from factories, monitoring oxygen concentration in breath or its content in marine ecosystems, combustion analysis in cars, etc. [3]. Some broader topics include applications,

for example, determining tissue structure in the biomedical sciences sector and astronomy, where it's used to study the physical properties of celestial objects [4].

While many of these detections rely on equipment based on the principles of non-dispersion infrared spectroscopy; however, those techniques are not calibration-free and require better sensitivity [1]. Wavelength modulation spectroscopy emerges as a valuable alternative technique, leveraging tunable diode laser sources since the early 1970s to increase sensitivity [5]. It provides long-term stability and self-monitoring and has been used for trace gas detection in environmental and industrial applications [6] [7]. All these characteristics have made WMS a versatile technique and used for various gases with detection limits in the ppb·m or ppm·m. Continuous research efforts are underway to improve both the hardware and measurement aspects of WMS, promising its refinement and use in various fields.

Furthermore, researchers often employ a multipass cell in WMS experiments for trace gases, such as a Herriott multipass cell named after Doland R. Herriott [8], in WMS systems. The optical cell facilitates a long interaction distance with the gas sample and the laser light while keeping the system's distance reasonable [9]. This cell is used in a WMS optomechanical setup to increase the effect of a weak or low-concentrated gas. In cases where the gas's signal is too weak to observe in one pass but in > 10 passes, the signal-to-noise ratio is much better [9]. Observing the spectra of gases with low concentrations poses a challenge. Any additional optical interference will likely decrease the signal-to-noise ratio, thereby impacting the accuracy and sensitivity of the measurement. While the amount of scattering or interference within the cell may be minimal, it's crucial to acknowledge that even a slight optical interference can substantially impact the signal. Therefore, to ensure accuracy and sensitivity in the technique, we have designed masks to suppress optical fringes in the cell. Assumed reasons for scattering will be discussed in Chapter 2. To reduce scattering in the cell, we created masks in MATLAB and FRED software for simulations and tested them experimentally.

Chapter 2

Wavelength Modulation Spectroscopy

Wavelength modulation spectroscopy (WMS) is a well-known and refined technique for sensitive and accurate gas sensing measurements. WMS offers enhanced selectivity in detecting trace gases, efficient noise suppression, specifically reduces the to 1/f noise, eliminates the laser amplitude modulation in the data, and can operate over a wide range of gas concentrations [1]. WMS capitalized on subtle gas concentration variations by modulating the laser wavelength, enhancing sensitivity and precision.

Despite its advantages, WMS's absorption measurements are susceptible to optical interference from within the optical cell. The scattering rays from the cell can interfere with the signals, potentially affecting the accuracy of the measurements. It's crucial to minimize the scattering, and Hong Chang has done it by using a mask along the surface of a toroidal absorption cell [10]. Our experiment used a Herriott multipass cell and designed masks to mitigate scattering.

2.0.1 Spectroscopic Modeling

We used a 763 nm vertical cavity surface emitting laser (VCSEL), which is tunable over 10 oxygen absorption lines. We targeted a couple of these lines to perform sensitive oxygen spectroscopy. The laser's wavelength can be adjusted by its temperature and current.

However, temperature tuning is directly due to self-heating. The laser is mounted on a thermoelectric cooler, enabling adjustments of temperature from 10 $°C$ to 40 $°C$. Temperature is monitored by an in-built thermistor with its resistance value in $k\Omega$. There's a direct correlation between the thermistor's resistance and the laser temperature. The conversion formula for thermistor resistance R (Ohm) to laser temperature T (Kelvin) is given by [11]:

$$T = (T_0^{-1} + ln(R/R_0)/\beta)^{-1} \tag{2.1}$$

where R_0 represents the resistance of the thermistor at reference temperature T_0 (often T_0 =298.15K and R_0=10$k\Omega$) and β a specific constant (for this lab, $\beta = 3892$) [13]. Since we will only be tuning the laser current, we won't consider temperature tuning of the laser and will assume that $T = 296K$.

2.0.2 Molecluar Lineshape Background

Beer-Lambert law can be used to describe the transmission of a gas,

$$T(\nu) = e^{-\alpha(\nu)L} \approx 1 - \alpha(\nu)L, \text{ for low absorbance } \alpha L \tag{2.2}$$

where $\alpha(\nu)$ is the absorption coefficient (unit $\frac{1}{m}$), L is the optical path length (unit m) which is the length of light-gas interaction, and ν is the light's wavenumber (unit cm^{-1}) [12].

The absorption coefficient, $\alpha(\nu)$, is given by;

$$\alpha(\nu) = S^{'} c_{rel} p \chi(\nu) \tag{2.3}$$

where $S^{'}$ is the gas line strength ($cm^{-2}atm$), c_{rel} is the absorbers' relative concentration, p is the gas pressure (atm), and $\chi(\nu)$ is the area-normalized absorption lineshape function. Spectral lines in absorption spectra are neither inherently monochromatic nor precisely

"sharp". This is due to the finite lifetime of the states and the principle of energy uncertainty. These characteristics produce a broadening in absorption lines.
Moreover, due to molecular transitions, absorption occurs at a range of wavelengths and is dependent upon factors such as temperature and pressure. The lineshape function is utilized to mathematically depict this absorption distribution around the central frequency of the transition [13]. Three common lineshape models used in WMS are Gaussian, Lorentzian, and Voigt profiles [14].

Gaussian Model

The Gaussian lineshape is utilized to describe thermal motion in gas molecules resulting in Doppler broadening. The molecules undergo the Doppler effect which causes the spectral lines to broaden. When molecules possess a velocity component aligned with the propagation direction of the incident light, their absorption frequency undergoes a minor change [13]. Therefore, these molecules don't absorb at the frequency ν_0 but at a modified frequency $\nu_0(1 \pm \nu_z/c)$, where c is the speed of light (m/s). In mathematical terms, the Gaussian form is given by;

$$\chi_G(\nu_d) = \sqrt{\frac{4ln(2)}{\pi}} \frac{1}{\delta\nu_D} \exp\left\{ \frac{-4ln(2)\nu_d^2}{\delta\nu_D^2} \right\} \tag{2.4}$$

where $\delta\nu_D$ is the Doppler width of the Gaussian profile (cm^{-1}) and ν_D is the laser frequency detuning (cm^{-1}). The Doppler width of a spectral line is given by:

$$\delta\nu_D = 7.162 \times 10^{-7} \nu_0 \sqrt{\frac{T}{M}} \tag{2.5}$$

where ν_0 is the frequency of an atom at rest, T is the temperature (K) and M is the molar mass of the gas (g/mol) [14].

Lorentzian Model

In contrast, the Lorentzian lineshape is useful when atoms or molecules undergo collisions that alter the energy levels of the involved absorbers, resulting in pressure broadening. This occurs in dense environments with high pressure hence, increasing the likelihood of collisions. As a result, this causes homogeneous broadening of the absorption profile and leads to the form of Lorentzian lineshape, written as;

$$\chi_L(\nu_d) = \frac{1}{\pi} \frac{\delta\nu_L/2}{(\nu_d)^2 + (\delta\nu_L/2)^2} \tag{2.6}$$

where $\delta\nu_L$ is the broadened full-width-half-maximum lineswidth of the model (cm^{-1}) [14]. The pressure-broadened FWHM linewidth is given as such;

$$\delta\nu_L = 2\sum_i \gamma_i p_i \tag{2.7}$$

where γ_i represents the pressure broadening coefficient (cm^{-1}/atm) for i species, and p_i is its partial pressure (atm).

Voigt Model

The Voigt lineshape is a comprehensive model combining both Gaussian and Lorentzian lineshapes. It's used in experiments where various broadening mechanisms have affected the spectral lines. Unlike Gaussian and Lorentzian models, the Voigt profile cannot be computed analytically. It needs numerical modeling but for simplicity, it can be expressed as a convolution of both models;

$$V(x) = \int_{-\infty}^{\infty} G(x') \cdot L(x - x')dx' \tag{2.8}$$

where G(x') is the Gaussian profile, and L(x) is the Lorentzian profile [15].
Understanding these different lineshapes is crucial for the precise characterization of spec-

tral features in WMS. The model directly affects the accuracy and sensitivity of the measurements. The Voigt lineshape emerges as a useful profile as it combines the effects of Doppler and pressure broadening, which are common in real-world environments.

Lock-In Detection

Lock-in detectors extract weak signals from noisy backgrounds. It operates by modulating the signal of interest with a reference signal at a known frequency, we used a sinusoidal waveform. The modulated signal then passes through a narrow-bandwidth filter, which only amplifies the signal's parts corresponding to the modulation frequency. It can reject noise at frequencies other than the reference frequencies. It offers high sensitivity and selective detection for environmental monitoring and biological sensing [16]. Lock-in amplification is a synchronous homodyne detection that mixes the signal of interest, $a(t)$, and the reference signal, $b(t)$, as such;

$$a(t) = A\sin(wt + \phi) \tag{2.9}$$

$$b(t) = B\sin(\gamma t + \alpha) \tag{2.10}$$

By using a multiplicative trigonometric identity and matching the phase and frequency ($w = \gamma$, $\phi = \alpha$) of the signal:

$$a(t) * b(t) = AB * \frac{1}{2}(\cos[(wt + \phi) + (\gamma t + \alpha)] + \cos[(wt + \phi) - (\gamma t + \alpha)]) \tag{2.11}$$

$$= AB\frac{1}{2}(\cos(2wt + 2\phi) + 1) \tag{2.12}$$

Then, the signal is passed through a low pass filter to get a DC signal with an amplitude of $\frac{AB}{2}$ [12].

2.0.3 Gas Cell

A Herriott multipass cell was used to increase the optical path length and the sensitivity of the detection of trace gases. It is often used in laser spectroscopy to improve absorption in a system. It comprises two gold-plated resonators between which the laser beam goes through multiple reflections as it oscillates back and forth [8]. This enhances the interaction time between the light and gas molecules. The 100 cm focal length mirrors have acentric holes where light enters through one end and exits through either the same hole or from a hole through another mirror. A path length of 3.4 m was chosen, which resulted in 21 total passes. The increased path length ensures better absorption and a higher signal-to-noise ratio.

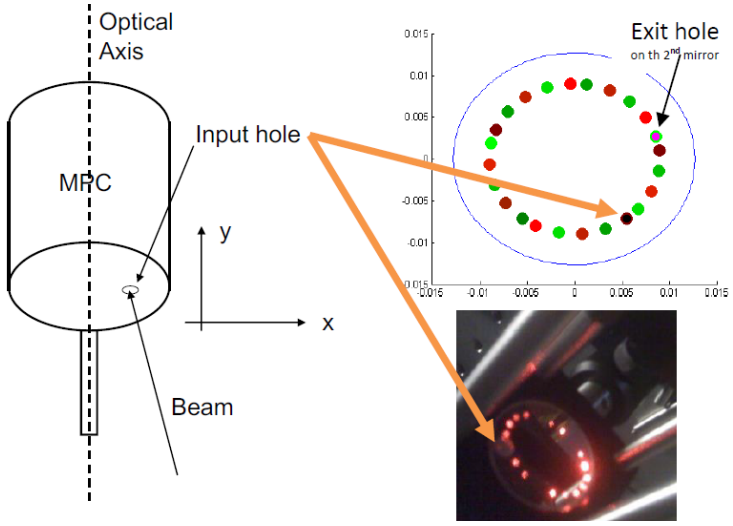


Figure 2.1: (Left) Diagram depicting beam coupling and coordinate axis of the Herriott type multi-pass cell. (Right upper) A simulated laser beam's spot pattern on a 3.6 m optical cell mirror is shown. (Right lower) Photograph of a mirror shown [12]

.

By changing the spacing between the mirrors and the incident angles of the beam, we can change the number of passes we observe on the mirrors. So, by allowing light to travel multiple times in the cell, we can increase the absorption length, hence increasing the signal we measure. The beam doesn't enter at 90 ° to the mirror; instead, it enters at some angle shifted in the x and y direction for it to have a circular pattern. Figure 2.1 shows a

schematic of the cell on the left, where light enters the cell through the input hole. On the right, we have a simulated image of the combined spot patterns on a mirror and a photographed picture of a 3.6 m cell.

2.0.4 Experimental Method

Set-Up

The setup for our WMS system is shown in Figure 2.2. The WMS system consisted of a laser, a current and temperature controller, a signal generator, an optical instrument for light interaction with gas (Herriott multipass cell), a photodetector, a lock-in amplifier, a 30 dB attenuator, and tuning mirrors. A 763 nm tunable VCSEl was used to illuminate the cell.

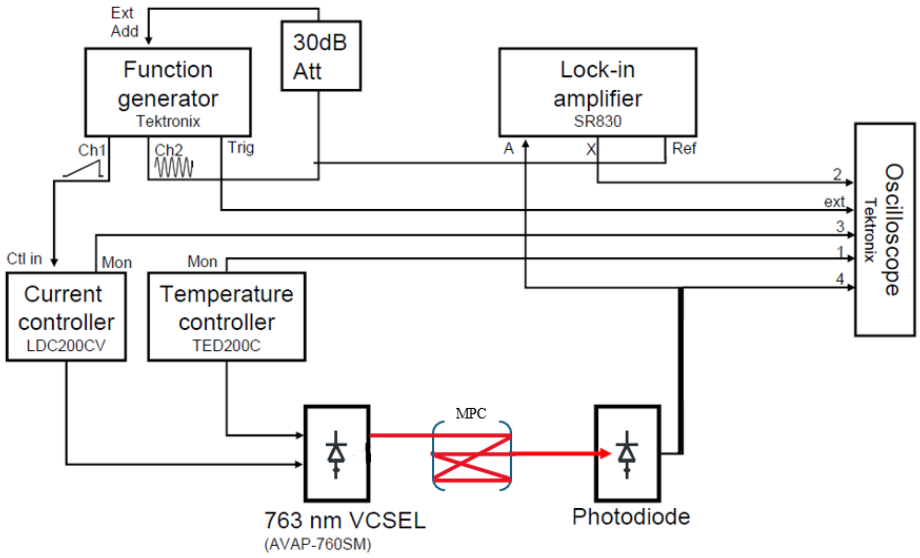


Figure 2.2: General schematic of a WMS system. The following pieces of instruments are used in the figure: function generator, temperature controller, laser current controller, oscilloscope, lock-in-amplifier, photodiode, multipass cell (MPC), and 30 dB attenuator [12].

A ramp and high-frequency sinusoidal modulation are superimposed on the laser injection current to implement WMS. Detection frequencies as low as 20 kHz are often sufficient to be out of the 1/f noise regime [1]. This current modulation, ramp, produces a modulation

of the laser wavelength since the wavelength is tuned by changing the current. Then, the laser is transmitted through the multipass cell, and a detector measures that signal. The lock-in amplifier uses the sine modulation's frequency to demodulate the detector signal into its harmonic components. To obtain the second-harmonic spectrum, the intensity at $2f$ is divided by the intensity at DC, so the effect of the laser amplitude is removed. Although there can be noise from certain pieces of equipment, the Herriott multipass cell is the potential source of optical interference, as we will see in Chapter 2. The fringe noise lowers the signal-to-noise ratio and decreases the detection sensitivity.

2.1 Optical Interference Noise in WMS Measurements

The Herriott multipass cell is based on the characteristics of a Fabry-Perot interferometer. Light undergoes multiple reflections between two highly reflective but partially transmissive mirrors in a Fabry-Perot interferometer, leading to interference phenomena [17]. As shown in Figure 2.3, light enters through one surface and exits through the other, and the reflected beams allow only selected rays to exit, which occurs due to interference. The rays have traveled different optical paths, which, when combined, lead to interference fringes on the detector. These fringes occur due to constructive and destructive light interference within the cavity.

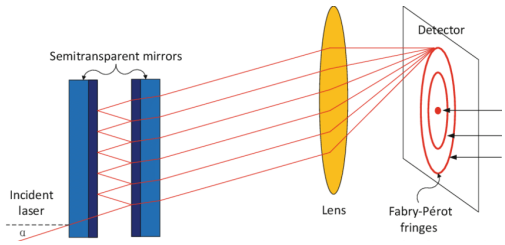


Figure 2.3: Fabry-Perot Interferometer, using a pair of highly reflective, semi-transparent mirrors

Similar to a Fabry Perot interferometer, a Herriott cell utilizes the concept of multiple reflections and interference fringes. Fringes can be produced from various sources such as the

lock-in amplifier or the laser [18], and partially reflective mirrors that have multiple passes. However, in our system, we suspect fringes to exist in the cell. Essentially, light has two paths to the detector where. One is the laser beam, and the other is from the scattered light. Figure 2.4(a) shows fringes appearing in the data in the zoomed region. This periodic nature of fringes is a drawback of WMS system measurements. It's essential also to mention that the cell is open to air, and the mirrors are gold-plated. Gold is a relatively softer metal used for mirror plating compared to aluminum and or silver [19]. Therefore, gold-plated mirrors are more sensitive, require more careful handling, and are more likely to collect dust. These dust particles scatter light in all directions, and those rays' interference produces fringes. Additionally, the interference of overlapping laser beams on the mirrors' surfaces is impossible to avoid altogether [9].

To suppress this optical fringe effect, we propose making an absorption mask and placing it in the cell to reduce the scattered light reaching the detector.

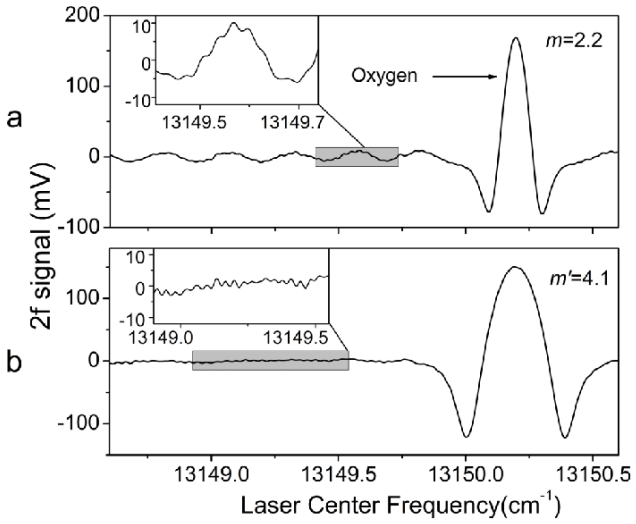


Figure 2.4: Second harmonic signal of O_2 in ambient air. Spectra were averaged 100 times over 10 s [20].

2.2 Multi-Pass Cell Simulations

2.2.1 Numerical Simulations of Multi-Pass Cell using MATLAB

Understanding how the beam propagates within the cell is paramount in designing a mask. Utilizing MATLAB code developed by Jonas Westberg and Michael Soskind, we estimated the entry beam angles in the x and y planes. This theoretical model also produced expected beam locations on the two mirror surfaces. It's important to note that the beam doesn't enter the cell perpendicular to the mirrors in the cell. Instead, the beam must meet specific angles to satisfy the re-entrant condition Equ.(2.13). Aligning the beam within the cell requires an initial estimate of its path, achieving the ultimate goal of obtaining a circular spot pattern. The calculations are based on the re-entrant condition Equ.(2.13), which dictates that the product of total reflections (N) and the angle between successive reflections (θ) must be an integer multiple of 2π to exit the Herriott cell [8]. We estimated the incident angles at the beam that should enter the cell to start the alignment process. With the chosen length of the cell, we have 21 passes in total, as shown in Figure 2.5. On the right is the plot with even passes, including the entrance one, and the left plot has all the odd passes.

$$N\theta = 2\pi M, \quad M = 1, 2, 3 \tag{2.13}$$

This numerical method was a good first-order approximation as it gives us a rough estimate of what to expect when we run the simulations with the specific parameters.

2.2.2 Ray Tracing Software

FRED is photon engineering software for ray tracing and designing optomechanical systems. It was used to simulate and design the mask in the optical cell. The incident angles and cell length provided by the MATLAB code were used to trace the beam's path and

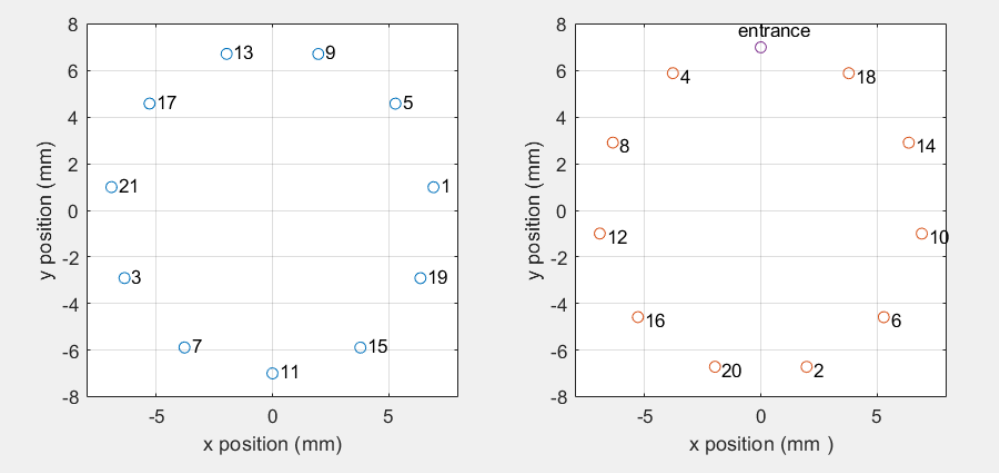


Figure 2.5: Spot positions for front and back mirrors using MATLAB. (Right) even spot patterns, including the first pass into the cell. (Left) There are odd spots with the 21st pass as the last pass.

design the Herriott cell.

FRED was used to simulate and design the optomechanical WMS system intricately. Precision in light propagation was achieved through iterative simulations and analyses within the FRED environment, and the overall system's optimal performance was ensured. This systematic use of FRED expedited the design process and showed the robustness and efficiency of the final optomechanical solution in simulations. Figure 2.6 shows the ray tracing simulation between two gold-plated, spherical mirrors in FRED. The spot pattern is created on the mirrors' surfaces and captured on an analysis plane. The software has various light sources to choose from, and we decided a coherent laser beam with its starting point outside of the front mirror.

An analysis plane was placed on the surface of the back mirror to get the spot pattern. However, a FRED script was equipped to get the total intensity plot of the spot pattern of the beam on the mirror surfaces. FRED's scripting language uses WinWrap, which is based on Visual Basic and is used to automate iterative ray tracing and model creation process [21]. The script iterates through each spot by adding up the intensity and produces a plot of the total intensity of the beam on the analysis plane. Figure 2.7 shows the spot pattern captured on the analysis plane when the script was run.

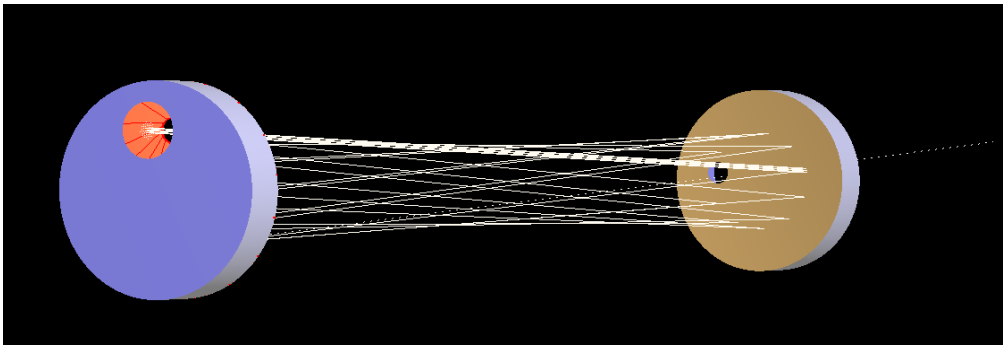


Figure 2.6: Ray tracing of a laser beam in FRED. There are a total of 21 passes within the cell.

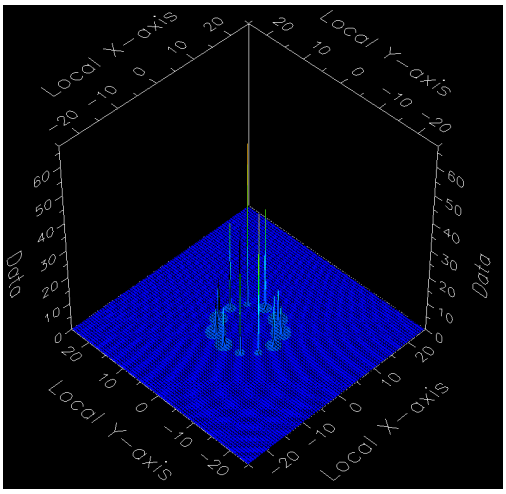


Figure 2.7: Spot pattern on the back mirror using FRED script.

The script was built to verify the MATLAB results and visualize the different spot sizes by adding the irradiance after each pass.

2.3 Suppressing Scattering in Herriott Multipass Cell

2.3.1 Simulating Scattering

This project aimed to suppress scattering within the optical cell, more specifically, to minimize the contribution of light from one spot to other spots. We simulated the impact of scattering using the FRED software to evaluate the effect of scattering. Rays intended for their designated spot positions on the mirrors are experiencing interference from scattered

light, which is undesirable. Point sources were utilized as proxies for scattering sources. As shown in Figure 2.8, diffused light emanates in multiple directions, resembling scattered light, and has a wider angular cone than direct light. This is similar to when light rays hit dust particles. Figure 2.8 illustrates the difference between diffused reflection, scattered light, and specular reflection.

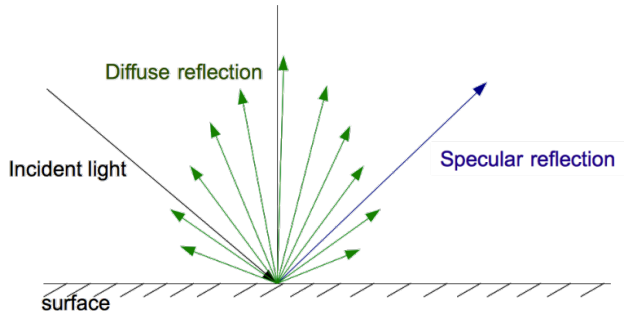


Figure 2.8: This figure shows the difference between diffuse and specular reflections. When the rays hit dust particles or irregularities on the mirrors, light is scattered in all directions [22].

A point source was placed on one of the mirror surfaces at each of the spot positions to mimic scattering from each spot. Figure 2.9 shows the front mirror with point sources. There's a source at the entrance spot because the first pass can also create interference with the laser beam after multiple passes.

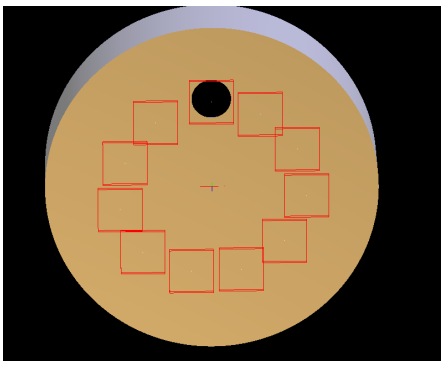


Figure 2.9: Point sources are located on the mirror corresponding to the spots' positions. Each point source is positioned at the center of the red squares. It's worth noting that the red squares indicate the selection of point sources clicking.

Figure 2.10 shows one point source turned on, and we can see the conical shape of light. Two assumptions were made: an analysis plane was placed in front of the other mirror

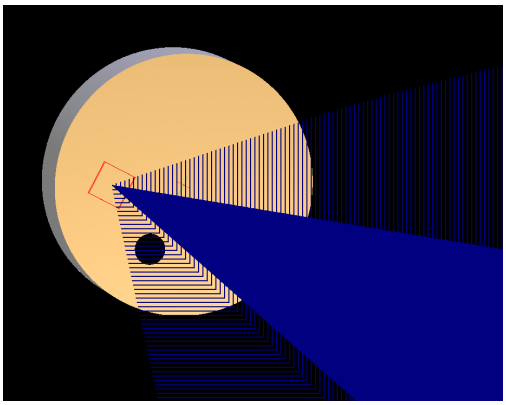


Figure 2.10: One of the point sources is turned on to see how it casts light uniformly and in all directions. The point source exhibits specific characteristics, including an angular spread cone of 20° and 500 angular zones over the angular spread.

that calculated the irradiance (intensity/area) for all the rays, and the point sources were halted after 1 pass. To minimize scattered light, we want to design masks in the system to model the effects of interference on a plane.

2.4 Mask Design and Optimization

2.4.1 Design of a Mask Pattern and Placement

Using the results from the Matlab code, we approximated the location of holes on a mask, depending on where it is placed along the cell's trajectory. It's important to show how the holes were created. Figure 2.11 shows how the hole is made on the piece of material along the cell's length. A hole is created at that spot, so a mask was created using each beam passed throughout the cell. The hole size was adjusted to make sure no part of the beam was being cut by the mask. The total irradiance of the beam was measured before and after each pass as well.

There were three final mask designs and placements in this thesis. The first one is a theoretical mask, as it explains the ultimate goal of designing a mask, which is only to illuminate the destination spots of the beam. This is shown in Figure 2.12. The idea is similar to looking through a straw and only seeing the destination spot. Now, this is the only spot

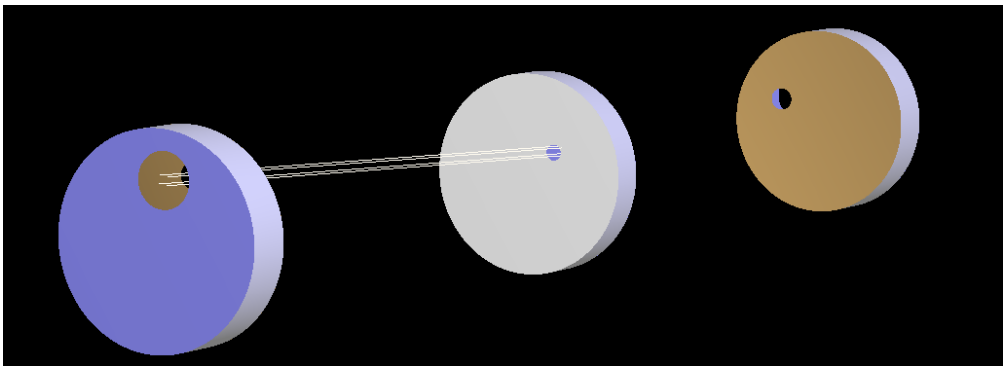


Figure 2.11: Ray tracing of a laser beam to design mask. This process was iterated for each pass until all the rays passed through the holes.

illuminated by the light. All the unwanted scattered light will get blocked or absorbed by the surface, in this case, a straw. This would be the end goal of design as it gives ultimate results by blocking all the scattered light. However, it's not practical to make this mask because of the uneven distribution of gas in each hole, and it is unfeasible to align the holes to the beam to avoid clipping perfectly. So, we want to come as close to that idea by using as few masks as possible.

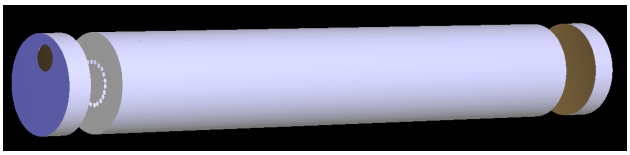


Figure 2.12: This is a theoretical mask created to visualize a mask with zero scattered light contributed from neighboring spots. This is impractical, but getting as close to it as possible is the idea.

The final idea that we went ahead with was to make some mask(s) and place them along the path of the gas. The next was to test its effectiveness against scattering.

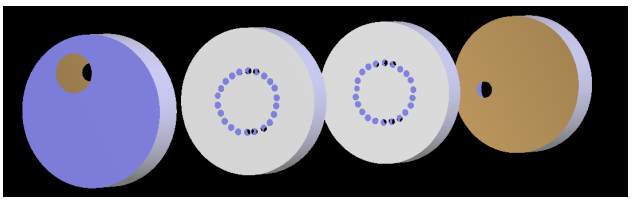


Figure 2.13: 2 masks: one at 1/3 distance from the first mirror and the second one at 2/3 distance from the first mirror.



(a) Without Mask (b) With Mask

Figure 2.14: Irradiance distribution on an analysis plane in front of the back mirror with all point sources enabled. 78% decrease in scattered light after the addition of mask.

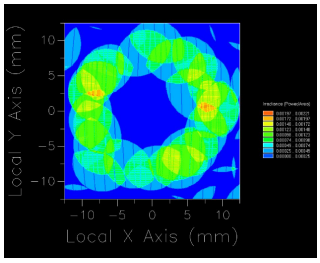
Figure 2.13 shows 2 masks placed at 1/3 and 2/3 distance apart from the front mirror. We considered this idea, but first, we wanted to experiment with one mask in the system. See Chapter 3 for more details.

2.4.2 Scattered Light Simulations with Mask

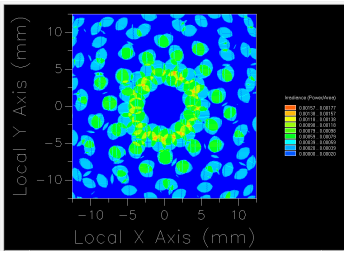
With the addition of a mask in the middle of the cell, we noticed a significant reduction in scattered light reaching the analysis plane placed on the surface of the back mirror. Figure 2.14 compares irradiance distributions of all point sources without and with a mask in the middle when all the point sources are turned on.

2.4.3 Mask Placement

We have observed noteworthy results through extensive simulations with various mask configurations within the cell. While numerous configurations were tested, a singular example highlights the efficacy of positioning the mask centrally within the cell. This positioning demonstrates superior performance compared to alternative placements, as evidenced by the identical scattering profiles from both mirrors when the mask occupies the central position in Figure 2.15. Additionally, an observable reduction in total power on the analysis plane is evident when the mask is positioned centrally within the cell instead of 20mm from the front mirror in Figure 2.15 (a). Specifically, only the central placement of the mask yields the least amount of scattered light captured on the analysis plane and



(a) Mask at 20 mm from front mirror. Relative power: 0.1256 units.



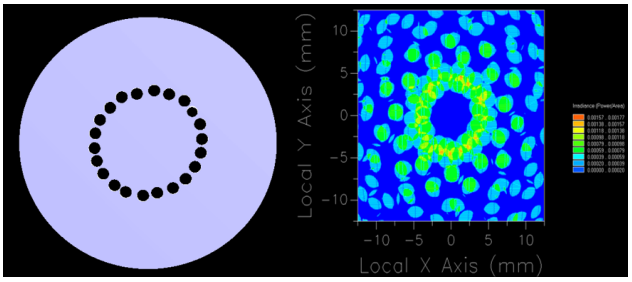
(b) Mask in the middle of cell. Relative power: 0.0619 units.

Figure 2.15: Total irradiance on an analysis plane for both front and back mirror. The mask is placed at different locations with all point sources turned on.

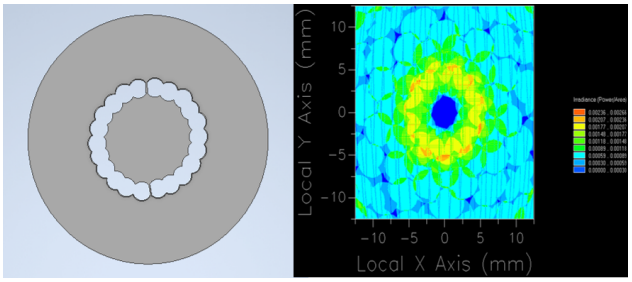
without a significant reduction in the beam's intensity. These plots are in a 2-D perspective view where x and y axes represent the position of the rays and z is the intensity of the beam. There's a color legend representing the intensity of light captured on the plane. Visually, it is apparent that the plane with the mask at 20 mm exhibits significantly higher traces of green and yellow color than the plane with the mask in the middle. Furthermore, the calculated total relative power on the analysis plane for the 20 mm mask was twice as high as that of the mask in the middle.

2.4.4 Optimization of Mask Design

After simulating the mask and quantitatively confirming a reduction in scattered light on the mirror's surface in FRED, it is important to consider design challenges in the experimental setup. Mask 1.0, as depicted in simulations in Figure 2.16a, was designed for preliminary testing. This mask is difficult to implement since it needs more precise rotation for all passes in the cell. Mask 2.0, shown in Figure 2.16b, is a simpler version where the holes were a little bigger, and the thickness was reduced to 1mm to allow more flexibility in the experimental setup. However, with bigger holes, more scattered light will end on the plane. This is shown in Figure 2.16b, where there's more scattered light on the analysis plane than in Figure 2.16a. Mask 2.0 blocks about 8% less light than Mask 1.0. After the masks were tested in FRED, they were designed in Inventor Professional.



(a) Mask 1.0 and its intensity distribution. This mask is 5 mm thick with a hole size of radius of 0.5 mm.



(b) Mask 2.0 and its intensity distribution. This mask is 1mm thick with holes' of radius 1mm.

Figure 2.16: Mask 1.0 & 2.0's intensity distribution. Mask 2.0 blocks about 8% less scattered light than Mask 1.0.

We chose to simplify the mask design due to the disparity between the numerical outcomes from the code and the actual experimental setup. The mask needed a higher tolerance to accommodate the beam to pass through the mask without any obstruction. Moreover, while the MATLAB code provided initial estimates of beam propagation to initiate beam alignment within the cell, achieving a circular spot pattern in the experiment necessitated fine-tuning the mirrors. This implied alterations to the incident angles of the beam. Consequently, the simpler mask emerged as the optimal choice, as the mask with holes was found to clip the beam.

We proceeded to refine the mask further. Figure 2.17 shows the mask's final design utilized for experiments. While it does block 8% less light than Mask 2.0, its implementation and 3-D printing are more straightforward.

We used Inventor Professional, a version of computer-aided design (CAD) software, to create a mask design. Then, the CAD model was exported to a 3-D printer, which converted

the mask design into a physical object layer by layer using plastic. Finally, some smoothing was performed using sandpaper to the edges to ensure the mask was ready for use in the experimental setup.



Figure 2.17: A more simplified mask shown in FRED. Blocks about 8% less light than Mask 2.0 but easier to implement.

It is noteworthy that the final mask design underwent numerous iterations of trial and error. This was primarily to rectify beam clipping issues resulting from the disparity between numerical and experimental systems, as mentioned earlier. Furthermore, this refined design is expected to be particularly effective for increasing the number of passes when analyzing trace gases.

2.5 Experimental Setup with Mask

To seamlessly run the experiments, it was crucial to place an optic mount in the middle of the cell so we could easily put on and remove the mask. Figure 2.18 is a picture of the mask within the cell. The 763 nm VCSEL was transmitted into the cell using 2 steering mirrors, and the mask was rotated and adjusted to ensure no part of the beam was clipped. The beam exited the cell and went to the detector. A lock-in amplifier was used to get the second harmonic ($2f$) signal, which uses the sine modulation's freq to demodulate the signal and remove the laser modulation amplitude. The $2f$ signal is recorded using a Data Acquisition (DAQ) card when a MATLAB code is run (see Appendix).

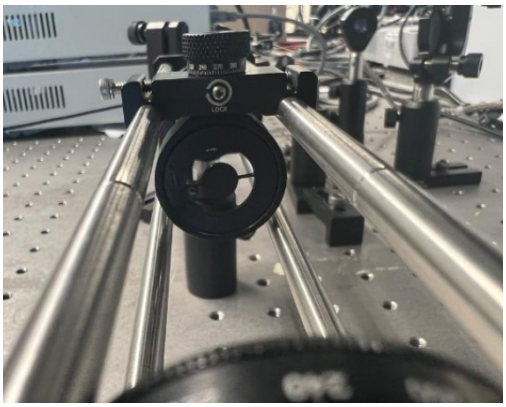


Figure 2.18: 3-D printed mask is held in place with an optic mount within the Herriott multipass cell.

Figure 2.19 shows a second harmonic signal that we measured without the mask and next to it is a zoomed-in image of the noisy fluctuations. The fluctuations could be noise from the laser, photodetector, or amplifier, but in this signal also resides the fringes from the multipass cell. Firstly, WMS employs harmonic detection to improve signal-to-noise ratio since the signal is modulated at a specific frequency. Secondly, the lock-in amplifier amplifies the weak signal at the modulation frequency while suppressing the background noise and interference at other harmonics. Lastly, background subtraction at a nearby wavelength, unaffected by gas absorption, eliminates noise and fluctuations from the laser or detector. The limiting factor remaining is the unintentional formation of fringes in the multipass cell. The fringes appear as periodic oscillations in the measurements since they have a similar free spectral range to the absorption gas cell[9].

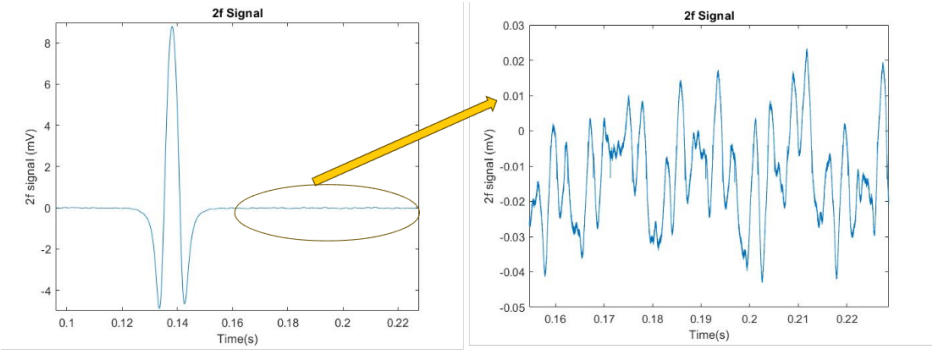


Figure 2.19: A more simplified mask shown in FRED. It blocks about 8% less light than Mask 2.0 but is easier to implement.

So, to find the contribution of this noisy signal, we had to calibrate the signal first. There are many ways to do the time-to-wavenumber conversion. One way is with a spectrum analyzer and an etalon. Another way that we utilized was to use the $2f$ signal to get the ratio of transition frequencies and look them up in HITRAN to identify peaks [23]. Figure 2.20 is the transmission spectrum, and the shape is from the ramping of the laser current. The measured gas absorption is the small dips in the plot. So, once we know the two transition frequencies, the corresponding time values can be extracted from the dips in the transmission spectrum. We could find a linear relationship between time and wavenumber. Using $2f$ detection we can extract the concentration of the gas with the time to laser detuning current. However, since, we are interested in the noise associated with the cavity length, calibration is necessary in .

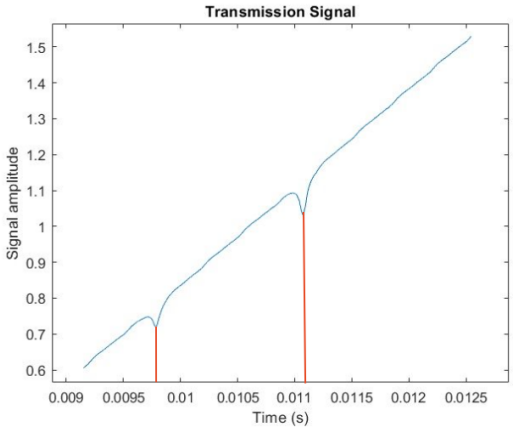


Figure 2.20: Transmission signal used to find the time values at dips.

The troughs observed in the transmission signal align with the peaks in the absorbance signal depicted in Figure 2.21. By assuming a linear correlation between time and wavenumber, we derive the slope utilizing the time values corresponding to the troughs and the respective wavenumber values from Figure 2.21. Leveraging this slope, we used the linear equation to convert the time scale into wavenumbers. Figure 2.21 is used from HITRAN at standard temperature and pressure (STP) and a path length of 340 cm [24].

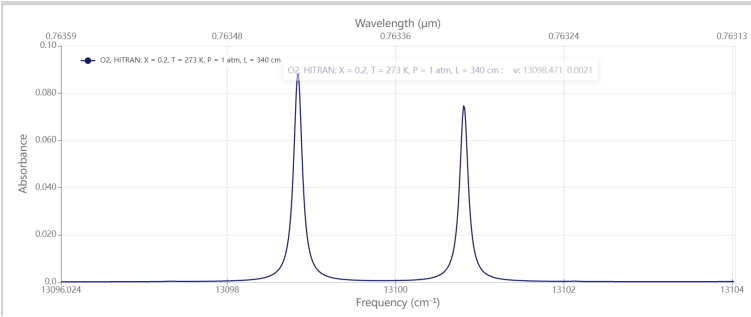


Figure 2.21: O_2's absorption peaks at 13098.37 and 13100.82 cm^{-1}, corresponding to the transition frequencies found in the experiment.

2.5.1 Noise Analysis

We aimed to transform the x-axis from time to wavenumber the signal's Fast Fourier Transform (FFT). This conversion allows us to represent the x-axis in terms of length (cm), which is useful to compare the path length within the cell for each pass. Figure 2.22 illustrates the noisy regime of the signal without a mask, plotted against wavenumbers on the x-axis.

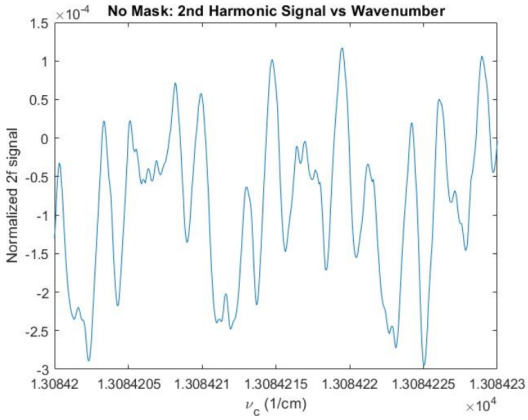


Figure 2.22: Noisy part of no mask signal with x-axis in wavenumbers.

By performing the FFT of the signal, we can express the x-axis in terms of length, which allows us to compare equipment distances relative to the optical cell. Figure 2.23 shows the normalized FFT of the noisy $2f$ signal with the orange plots without a mask and purple with a mask. Upon normalization, the FFT gives inconclusive results as the amplitude of the peaks in the signal with and without the mask are approximately equal. Con-

sequently, FFT alone does not clarify whether the mask effectively mitigates noise from the cell. So, to assess the contribution of noise from the cell, we can examine the number of instances where the noise originates by analyzing the difference in peak lengths.

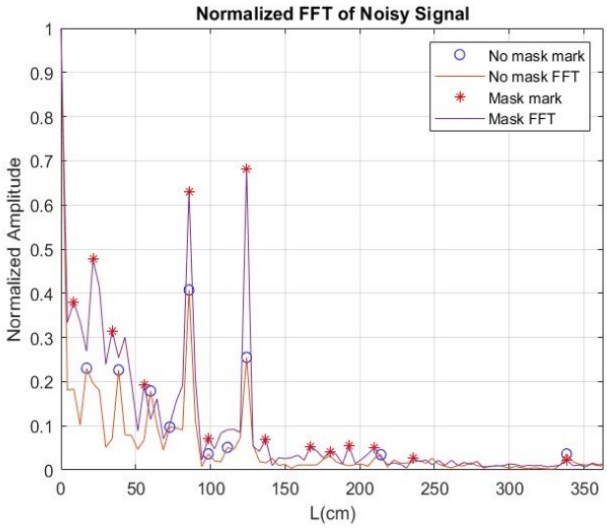


Figure 2.23: FFT of noisy signal with and without the mask. Normalized signal presenting distance components present in the fringes' signal. The signal is normalized to its DC component.

We are interested in finding the distance between adjacent peaks that are shown in Figure 2.23. To achieve this, we graphed the distance (cm) between each adjacent pair of peaks. The histogram in Figure 2.24 shows the total number of occurrences for various distance ranges within the system. For instance, in the absence of a mask, distances between 10 cm and 14 cm were recorded 14 times, whereas in a masked system, they occurred 12 times. If the distance between the peaks corresponds to about 17.1 cm, it implies the noise originated from the cell itself. Our objective is to determine whether this optical interference is reduced with the addition of a mask.

A lower occurrence of distances with the mask than without the mask, suggests that the mask successfully suppressed the noise associated with the cell's path length. The highlighted bin in the histogram is particularly relevant because it represents the noise aligned with the cell's path length. We observed a decrease in the number of instances of noise with the mask, which indicates the mask's effectiveness to some extent. Notably, the bins

are broad and are reasonably constrained by resolution. We conducted a Signal-to-Noise (SNR) analysis to further validate the mask's efficacy.

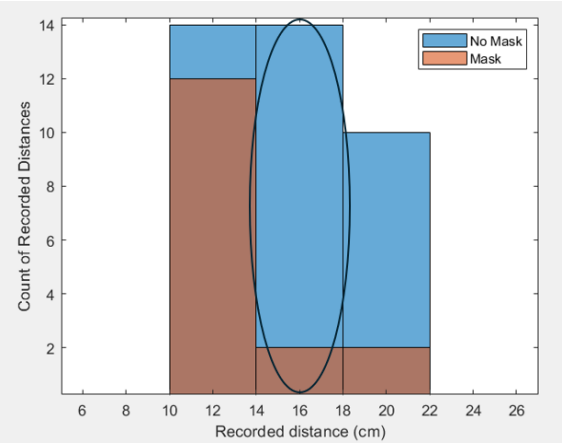


Figure 2.24: Histogram representing the number of noise instances corresponding to different distances in the system. The circled bin is for the multipass cell's path length of 17.1 cm.

2.5.2 SNR Analysis

Signal-to-noise (SNR) analysis is a crucial aspect of evaluating the performance of spectroscopic techniques such as Wavelength Modulation Spectroscopy [25]. It can give valuable insights into the effectiveness of noise reduction measures in a system. SNR is the ratio of the input signal to the level of noise in the system as shown in Equation 2.14. In the context of WMS, SNR involves measuring the amplitude of the second harmonic signal and comparing it to the level of noise present in the measurement.

$$\text{SNR} \triangleq \frac{\text{Input Signal}}{\text{Noise}} = \frac{I_p}{\sigma} \tag{2.14}$$

For the analysis, we utilized the peak-peak amplitude, I_p of the signal, and then calculated the noise signal's standard deviation,σ, to calculate the SNR. Figure 2.25 shows the 2 f signals with and without the mask, and despite the similarities in appearance, their σ values are different. SNR without the mask was calculated to be 864.60 units, and with the

mask was 920.75 units. The signal with the mask has a higher SNR than the one without the mask. This also shows that the mask was effective in reducing the noise in the signal and, therefore, improving the SNR of the signal.

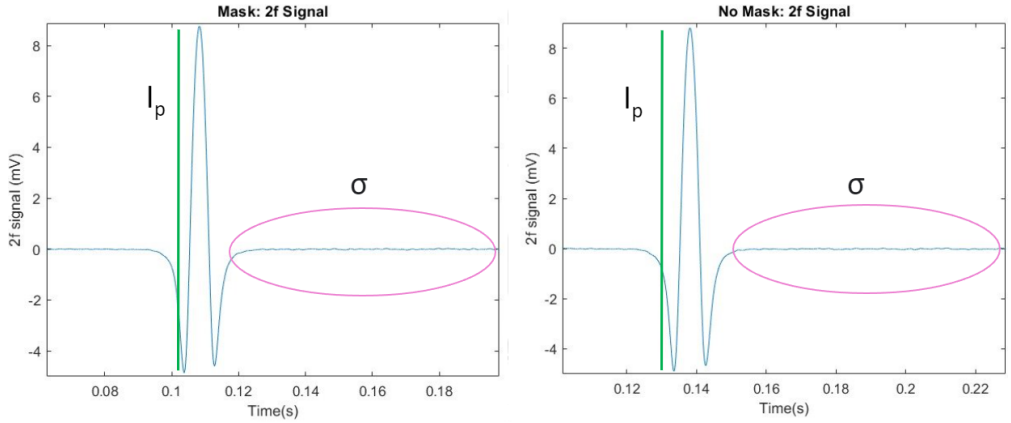


Figure 2.25: Second harmonic signals with circled areas were used for SNR analysis. (left) Mask, (right) No mask

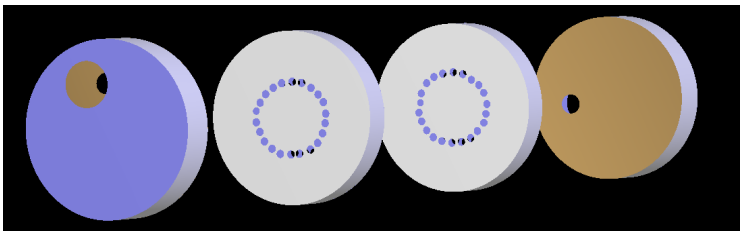
These initial findings serve as a foundation, but further investigation is necessary to validate the mask's efficacy. One potential step could be to use a trace gas, such as Nitrous Oxide (N_2O). A trace gas is suggested due to the comparable amplitude of the fringes in the signal, making it challenging to distinguish between the signal and the noise.

Chapter 3

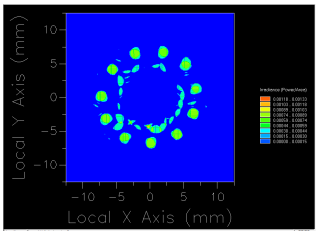
Conclusions and Future Directions

In this work, we examined the absorption masks in mitigating the effects of optical fringes in a WMS system for oxygen monitoring system. First, we leveraged theoretical knowledge of how light propagates in a Herriott multipass cell to tackle the problem numerically. We approximated the mirror surfaces' spot pattern and used it as an initial approximation in FRED simulations. FRED was employed for all the simulations from mimicking scattering to the validating of the final mask design. Following the successful simulations, we simplified the mask design to accommodate more passes for longer path lengths. Inventor Professional software was used to design and 3-D print a mask after numerous iterations. After experimental testing and data analysis, we determined that the mask successfully suppressed some fringes within the optical cell.

As noted earlier, these experiments and results are preliminary, and further work is required to demonstrate the mask's effectiveness conclusively. Analyzing the mask's performance with a trace gas rather than an abundant gas, such as oxygen, could provide better insights. Moreover, if we can successfully reduce fringes in this system, this could potentially lead to similar reductions in other systems. Furthermore, it may be beneficial to tune the laser temperature since improving the resolution of the second harmonic signal is crucial. We recommend adjusting the laser temperature and moving away from the transi-



(a) 2 mask in the optical cell



(b) With Mask

Figure 3.1: 2 mask system where the masks are 1/3 and 2/3 distance apart from the front mirror. Blocks 87% more scattered light than Mask 1.0 in Figure 2.16a.

tion frequency, which could potentially lead to finding more noise from the cell.

We also considered other concepts, such as drilling holes in a piece of material using a high-powered laser, eliminating the need for a predefined mask. This approach allows flexibility based on particular systems, and the mask can be made accordingly. Additionally, we considered placing two masks some distance apart in the system. Lastly, we are investigating the use of image processing techniques to create masks with carefully engineered holes to improve detection accuracy.

Figure 3.1 shows the FRED simulation outcomes with 2 masks strategically placed at 1/3 and 2/3 distance from the front mirror. The analysis plane in Figure 3.1b captures the scattered rays. As observed, there's a significant reduction in the amount of light getting to the back mirror with two masks compared to one. While avoiding the scattered light that goes along the beam's trajectory to reach the mirror is inevitable, we aim to minimize the amount of scattered light that bounces back and illuminates spots other than the intended destination. Further experimentation involving fabrication and optimization is required based on these initial results.

Next, we started the image processing method since it might produce a better approximation of the spot pattern than our numerical method. We started by sticking a piece of printer transparency in place of the mask and took a picture with an iPhone. Figure 3.2 illustrates the spot pattern captured, and the image's resolution is poor. Since the camera wasn't aligned with the plane of the mirrors, it needed some perspective and skew correc-

tions. Then, we used Keystone Corrector software in MATLAB to project the image in the same plane as the mirrors [26]. By selecting 4 corners of the transparency paper, we can correct the shift in angle from which the photo was taken. It's not perfect, but it does give us a better estimate of the spots. We can use that corrected image, extract a rough forecast of the spot position in place of a mask, and design a mask with those hole parameters. The picture in Figure 3.2 shows an example of the spot pattern visible on the paper. Resolution can be improved with a better camera and a small tripod for stability.

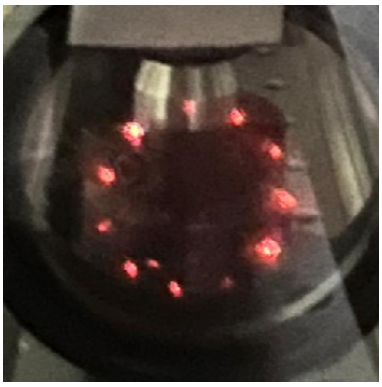


Figure 3.2: Spot pattern captured on the printer transparency paper using an iPhone.

Appendix A

Appendix

A.1 FRED Scripts

We developed this script to get the spot pattern on the mirror's surfaces.

```
'' Code for accumulating irradiances and saving that data to a .
   dat file


' Define the variables and structures as needed
Dim adv As T_ADVANCEDRAYTRACE
Dim ana As T_ANALYSIS
Dim srcID As Long
Dim snode As Long
Dim anode As Long
Dim temp() As Double
Dim irrad() As Double
Dim fname$, rcount&, icount&, count&


Sub Main
```

```
' Finding the names of the sources

srcID = FindFullName( "Optical Sources.Source 1" )
' srcID = FindFullName( "Optical Sources.Collimated Source
   " )
'snode = FindFullName( "Geometry.Target Plane_absorb_end
   2.Surface" )
snode = FindFullName( "Analysis Surface(s).Back Mirror
   Plane" )

'snode =FindFullName( "Geometry.Target
   Plane_transmit_middle.Surface" )
Const fname = "UPDATED_IrradAccum_back_mirror_mask"

' load data from the Analysis Surface and transform to
   local coordinates of measurement surface
LoadAnalysis snode, ana
SetAnalysisParameters 25,25, 501,501, False, ana
ana.posX = 0
ana.posY = 0
ana.posZ = 171.537

' defining the limits in x and y
xlim=ana.Amax-ana.Amin
ylim=ana.Bmax-ana.Bmin
```

```
InitAdvancedRaytrace adv          'initalize the Advanced
   Raytrace with default settings
adv.hitCount = 1                          'step one
   intersection at a time
adv.traceActiveSources = True    'create new rays first
   time
'adv.suppressSummary = True       'turn off raytrace
   summary

count=1                                'default count value
stepcount=0                           'zero step counter

While count<>0                    'loop until there are no
   more rays to trace

        ' determine if raytrace continues
        count=AdvancedRaytrace(adv)       'advance rays
           one intersection
        stepcount=stepcount+1                    'number
           of intersections traced

        Print "running trace "

        'calculate irradiance
        If stepcount = 1 Then
                rcount = Irradiance ( snode, snode, ana,
                   irrad() )
```

```
        'rcount = Irradiance (snode, snode, ana,
           irrad() )    'note: irradiance
           calculated in local coordinates of
           snode
Else
        icount = Irradiance (snode, snode, ana,
           temp() )
        'icount = Irradiance (snode, snode, ana,
           temp() )
        rcount=rcount+icount
                                              'running
            count of rays used in irradiance
           calculation
        Print rcount

        'accumulate irradiance values in irrad()
        maxIrrad = -1
        For j=0 To ylim
                For k= 0 To xlim
                        irrad(j,k)=irrad(j,k)+temp
                           (j,k)
                        If maxIrrad < irrad(j,k)
                           Then
                                maxIrrad = irrad(j
                                   ,k)
                        End If
                Next k
```

```
                Next j
                'Print maxIrrad
                'Print snode
                'Print anode
                'Print xlim
                'Print ylim

        End If

        adv.traceActiveSources=False    'set to Trace
           Existing for remainder of process
        adv.hitCount = 2                          'step two
            intersections at a time

Wend

DeleteRays 'delete rays upon completion to free up RAM

'write out irradiance calculation to PlotFile in user
   Current Directory
fileName = "C:\Users\14756\Desktop\Multipass cell\" &
   fname & ".dat"
Print fileName
WriteToPlotFile fileName, ana, irrad()

DisplayPlotFile( fileName, True )
```

```
End Sub
```

A.2 MATLAB Code

Here's the code we utilized for the numerical method, written by Jonas Westberg and Michael Soskind.

```
% Program to calculate spot positions for a Herriott cell (
    spherical)
% References:"Off-Axis Paths in Spherical Mirror Interferometers"
% "Folded Optical Delay Lines"
% "Multipass cell design for Stark-modulation spectroscopy"
% http://citeseerx.ist.psu.edu/viewdoc/download?doi
    =10.1.1.476.1726&rep=rep1&type=pdf

% Originally developed by Jonas Westberg, modified by Michael
    Soskind & Angela Mehta
% last modified: 08/24/2023

% clear workspace, variables and figures
clc
clear all
close all

% options
enable.display = 1;

% Mirror parameters
```

```
f = 100;                          % focal length [mm]
M = 5;                            % M-parameter
N = 22;                           % #passes
d = 2*f*(1-cos(2*pi*M/N));        % mirror separation [mm]
%disp(d)
theta = acos(1-d/(2*f));          % angle for every pass
x0 = 0;                           % x-position start [mm]
y0 = 7;                           % y-position start [mm]

% re-entrant condition
cond = N*theta-M*2*pi;            % re-entrant condition
fprintf('---- RE-ENTRANT CONDITION ----\n')
if cond>0.001
    fprintf('re-entrant condition not fulfilled!\n')
else
    fprintf('re-entrant condition fulfilled!\n')
end
if enable.display
    fprintf('---------- PARAMETERS ----------\n')
    fprintf('M \t\t\t\t= %d\n',M)
    fprintf('N \t\t\t\t= %d\n',N)
    fprintf('theta \t\t\t= %0.3g rad\n',theta)
    fprintf('focal length \t\t= %0.3g mm\n',f)
    fprintf('mirror separation \t= %0.3g mm\n',d)
    fprintf('total path length \t= %0.3g m\n',d*(N-1)/1e3)
end
```

```
% calculate incident angle for spherical beam pattern
alpha = atan(y0/(2*f) * sqrt((4*f-d)/d)); % incident angle
beta = -y0/(2*f);   % incident angle


% calculate spot positions for every pass
x = []; y = []; L = [];
x_mid = []; y_mid = []; % L_mid = [];
for i=1:N
    x(i) = x0*cos(i*theta) + sqrt(d/(4*f-d)) * (x0+2*f*tan(alpha))
       *sin(i*theta);
    y(i) = y0*cos(i*theta) + sqrt(d/(4*f-d)) * (y0+2*f*tan(beta))*
       sin(i*theta);
    if i == 1
        x_mid(i) = (x0 + x(i))/2;
        y_mid(i) = (y0 + y(i))/2;
    else
        x_mid(i) = (x(i-1) + x(i))/2;
        y_mid(i) = (y(i-1) + y(i))/2;
    end
    if i > 2
        L = [L 1/M * sqrt( (x(i-2)-x(i))^2 + (y(i-2)-y(i))^2)];
    end
end

% spot separation
sL = mean(L);
```

```
if enable.display
    fprintf('mean spot distance \t= %0.3g mm\n',sL)
end
%formatSpec = 'x_mid is %4.2f  and y_mid is %8.3f\n';
%fprintf(formatSpec,x_mid,y_mid)

% exit-hole angle
exit_angle = atand(x(end-1)/y(end-1));
if exit_angle<0
    exit_angle = 360+exit_angle;
end

% exit angles
alpha_exit = atan((y(end-2)-y(end-1))/d);
beta_exit = atan((x(end-2)-x(end-1))/d);

if enable.display
    fprintf('-------- Entrance angles --------\n')
    fprintf('alpha \t\t\t= %0.3g%c\n',alpha*180/pi,char(176))
    fprintf('beta \t\t\t= %0.3g%c\n',beta*180/pi,char(176))
    fprintf('---------- Exit angles ----------\n')
    fprintf('alpha \t\t\t= %0.3g%c\n',alpha_exit*180/pi,char
       (176))
    fprintf('beta \t\t\t= %0.3g%c\n',beta_exit*180/pi,char(176))
    fprintf('-------- Exit-hole angle --------\n')
    fprintf('exit-hole angle \t= %0.3g%c\n',exit_angle,char(176))
    fprintf('---------------------------------\n')
```

```
end

% plot results
figure
set(gcf,'pos',[300 500 800 400])
cmp = get(gca,'colororder');
title(sprintf('Herriott cell spot positions, M=%d, N=%d',M,N))
subplot(1,2,1)
hold on; box on; grid on;
for i=1:numel(x)
    if mod(i,2)
        plot(x(i),y(i),'o','color',cmp(1,:))
        text(x(i)+0.3,y(i)+0.1,sprintf('%d',i))
    end
end
axis([-y0-1 y0+1 -y0-1 y0+1])
axis('equal')
xlabel('x position (mm)')
ylabel('y position (mm)')
axis square

subplot(1,2,2)
hold on; box on; grid on;
for i=1:numel(x)-1

    if ~mod(i,2)
        plot(x(i),y(i),'o','color',cmp(2,:))
```

```
        text(x(i)+0.3,y(i)-0.1,sprintf('%d',i))
    end

end
plot(x0,y0,'o','color',cmp(4,:))
text(x0-1,y0+0.8,sprintf('entrance'))
axis([-y0-1 y0+1 -y0-1 y0+1])
axis('equal')
xlabel('x position (mm)')
ylabel('y position (mm)')
axis square;

%%
figure
plot(x,y)
```

Bibliography

[1] Jia Chen. *Compact Laser-spectroscopic Gas Sensors Using Vertical-cavity Surface-emitting Lasers*, volume 130 of *Selected topics of semiconductor physics and technology*. Walter Schottky Institut, Technische Universität München, June 2011.

[2] Mhanna Mhanna, Mohamed Sy, and Aamir Farooq. A selective laser-based sensor for fugitive methane emissions. *Scientific Reports*, 13(1):1573, January 2023. Publisher: Nature Publishing Group.

[3] Arnaud Cuisset, Dean S. Venables, Xiaoming Gao, and Hassen Aroui. Applications of Spectroscopy in Environmental Monitoring of Gases and Aerosols. *Journal of Spectroscopy*, 2016:2575782, June 2016. Publisher: Hindawi Publishing Corporation.

[4] Pritam Roy. Spectroscopy Sensing System Provides Efficient Monitoring of Nitrogen Dioxide in Flue Gas, August 2022. Section: Optics / Photonics News.

[5] Peter Werle. A review of recent advances in semiconductor laser based gas monitors. *Spectrochimica Acta Part A: Molecular and Biomolecular Spectroscopy*, 54(2):197–236, February 1998.

[6] Xin Zhou, Xiang Liu, Jay B. Jeffries, and R. K. Hanson. Development of a sensor for temperature and water concentration in combustion gases using a single tunable diode laser. *Measurement Science and Technology*, 14(8):1459, July 2003.

[7] Heiko Ganser, Wolfgang Urban, and John M. Brown. The sensitive detection of

NO by Faraday modulation spectroscopy with a quantum cascade laser. *Molecular Physics*, 101(4-5):545–550, February 2003. Publisher: Taylor & Francis _eprint: https://doi.org/10.1080/00268970210159460.

[8] D. Herriott, H. Kogelnik, and R. Kompfner. Off-Axis Paths in Spherical Mirror Interferometers. *Applied Optics*, 3(4):523–526, April 1964. Publisher: Optica Publishing Group.

[9] Joel A. Silver and Alan C. Stanton. Optical interference fringe reduction in laser absorption experiments. *Applied Optics*, 27(10):1914–1916, May 1988. Publisher: Optica Publishing Group.

[10] Hong Chang, Shiling Feng, Xuanbing Qiu, Huiyan Meng, Guqing Guo, Xiaohu He, Qiusheng He, Xiaohua Yang, Weiguang Ma, Ruifeng Kan, Christa Fittschen, and Chuanliang Li. Implementation of the toroidal absorption cell with multi-layer patterns by a single ring surface. *Optics Letters*, 45(21):5897–5900, November 2020. Publisher: Optica Publishing Group.

[11] John S. Steinhart and Stanley R. Hart. Calibration curves for thermistors. *Deep Sea Research and Oceanographic Abstracts*, 15(4):497–503, August 1968.

[12] Andreas Hangauer, Stephen So, Jonas Westberg, Jie Liu, and Gerard Wysocki. Wavelength Modulation Tunable Diode Laser Absorption Spectroscopy. (Laboratory Manual for ECE 550), 2023.

[13] Jonas Westberg. Faraday modulation spectroscopy : Theoretical description and experimental realization for detection of nitric oxide. 2013. Publisher: Umeå universitet.

[14] Wolfgang Demtröder. *Laser Spectroscopy Vol. 1: Basic Principles*. Springer Berlin, Heidelberg, 4 edition.

[15] H.O. Di Rocco. The exact expression of the Voigt profile function. *Journal of Quantitative Spectroscopy and Radiative Transfer*, 92(2):231–237, 2005.

[16] Principles of Lock-in Detection | Zurich Instruments, December 2019.

[17] Chao Wei and Lin Li. Acoustic emission and ultrasound monitoring in laser Micro/Nanofabrication. In Koji Sugioka, editor, *Handbook of laser micro- and nano-engineering*, pages 1979–2002. Springer International Publishing, Cham, 2021.

[18] H.L.T. Lee and R.J. Ram. Mode partition noise in vertical cavity surface emitting lasers. In *2001 digest of LEOS summer topical meetings: Advanced semiconductor lasers and Applications/Ultraviolet and blue lasers and their Applications/Ultralong haul DWDM transmission and Networking/WDM compo*, page 2 pp, 2001.

[19] Dr Rüdiger Paschotta. Metal- Coated Mirrors.

[20] Bo Xiong, Zhenhui Du, and Jinyi Li. Modulation index optimization for optical fringe suppression in wavelength modulation spectroscopy. *The Review of Scientific Instruments*, 86(11):113104, November 2015.

[21] Photon Engineering. Photon Engineering | Knowledge Base, October 2022.

[22] The Difference Between Reflection and Scattering | MISS C.Deng, December 2012.

[23] HITRAN online line-by-line search: 1. Select Molecules.

[24] Christopher S. Goldenstein, Victor A. Miller, R. Mitchell Spearrin, and Christopher L. Strand. Spectraplot.

[25] Filip Musiałek, Dariusz Szabra, and Jacek Wojtas. Time-efficient SNR optimization of WMS-Based gas sensor using a genetic algorithm. *Sensors*, 24(6), 2024. Number: 1842 tex.pubmedid: 38544105.

[26] JKMSMKJ (2024) . KeystoneCorrector (https://www.mathworks.com/matlabcentral/fileexchange/50971-keystonecorrector), MATLAB Central File Exchange. Retrieved May 8, 2024.